ACS Catalysis

Research Article

pubs.acs.org/acscatalysis

Size-Dependent Reaction Pathways of Low-Temperature CO Oxidation on Au/CeO_2 Catalysts

Shilong Chen, Liangfeng Luo, Zhiquan Jiang, and Weixin Huang*

Hefei National Laboratory for Physical Sciences at the Microscale, CAS Key Laboratory of Materials for Energy Conversion and Department of Chemical Physics, University of Science and Technology of China, Hefei 230026, China

Supporting Information

ABSTRACT: Via a comprehensive time-resolved operando-DRIFTS study of the evolutions of various surface species on Au/CeO_2 catalysts with Au particle sizes ranging from 1.7 ± 0.6 to 3.7 ± 0.9 nm during CO oxidation at room temperature, we have successfully demonstrated size-dependent reaction pathways and their contributions to the catalytic activity. The types and concentrations of chemisorbed CO(a), carbonate, bicarbonate, and formate species formed upon CO adsorption, their intrinsic oxidation/decomposition reactivity, and roles in CO oxidation vary with the size of the supported Au particles. The intrinsic oxidation reactivity of CO(a) does not depend much on the Au particle size, whereas the intrinsic decomposition reactivity of carbonate, bicarbonate, and formate species strongly depend on the Au particle size and are facilitated over Au/CeO_2 catalysts with large Au particles. These results greatly advance the fundamental understanding of the size effect of Au/CeO_2 catalysts for low-temperature CO oxidation.

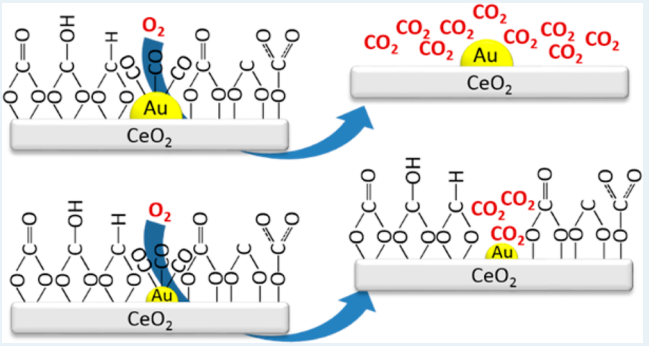

KEYWORDS: *Au catalysis, size effect, DRIFTS, reaction mechanism, surface species, hydroxyl group*

1. INTRODUCTION

Heterogeneous catalysis by gold has advanced significantly since Haruta et al. reported the very high catalytic activity of Au particles below 5 nm dispersed on base metal oxides in low-temperature CO oxidation.[1] The size-dependent catalytic activity of supported Au catalysts in CO oxidation is a fascinating fundamental issue in Au catalysis[2,3] and has been extensively studied.[4,5] The decrease in the size of supported Au particles increases the Au-support perimeter interface length and, thus, enhances the catalytic activity of supported Au catalysts following the periphery reaction mechanism.[5] The size of the supported Au particles can affect their geometric structure/morphology and, subsequently, the number of low-coordinated Au atoms generally with enhanced catalytic activity.[6−9] The decrease in the size of Au particles can also change their electronic structure, including the quantum size effect and, subsequently, the catalytic activity.[5,9] However, it has been recognized that CO oxidation catalyzed by supported Au catalysts follows various reaction pathways involving different active sites and the corresponding surface species/intermediates;[10−26] thus, the size-structure-catalytic activity relation established without adequate information on the surface species/intermediates and reaction mechanisms could be one-sided in fundamentally understanding the size effect of supported Au catalysts.

Diffuse reflectance infrared Fourier transformed spectroscopy (DRIFTS) and temporal analysis of product (TAP) techniques are powerful in identifying surface species/intermediates and elucidating reaction mechanisms of heterogeneous catalytic reactions. Au/CeO_2 catalysts are among the most extensively studied supported Au catalysts for CO oxidation. DRIFTS results have demonstrated the formation of various surface species, including CO(a) adsorbed on Au surfaces and carbonate, bicarbonate, and formate species involving CeO_2 surfaces upon CO adsorption on Au/CeO_2 catalysts[15,16,27] and the facile oxidation of CO(a) adsorbed on Au surfaces by O_2,[16,26,27] whereas TAP results have demonstrated the participation of carbonate, bicarbonate, and formate species involving CeO_2 surfaces in CO oxidation.[17] However, the size effect of Au particles supported on CeO_2 on the intrinsic reactivity of CO(a), carbonate, bicarbonate, and formate species has not been explored.

In the research for this paper, we prepared Au/CeO_2 catalysts with different Au particle sizes between 1.7 and 3.7 nm and employed the time-resolved operando-DRIFTS technique to comprehensively study the CO adsorption and oxidation processes on these Au/CeO_2 catalysts. The types and concentations of chemisorbed CO(a), carbonate, bicarbonate, and formate species formed upon CO adsorption were observed to depend on the size of supported Au particles;

Received: December 22, 2014
Revised: January 30, 2015
Published: February 3, 2015

DOI: 10.1021/cs502067x
ACS Catal. 2015, 5, 1653−1662

moreover, these surface species were observed to exhibit different dependences of their intrinsic oxidation/decomposition reactivity on the size of supported Au particles. These results reveal a novel vision on the size effect in supported Au catalysts for CO oxidation that the contributions of different surface species and corresponding reaction pathways to the catalytic activity depend on the Au particle size.

2. EXPERIMENTAL SECTION

2.1. Catalysts Preparation. All chemical reagents with the analytical grade were purchased from Sinopharm Chemical Reagent Co.; CO (99.99%), O_2 (99.999%), Ar (99.999%), and N_2 (99.999%) were purchased from Nanjing Shang Yuan Industrial Factory. All chemicals were used as received. CeO_2 was synthesized by precipitation using urea as the precipitation agent. Typically, 10.96 g of $(NH_4)_2Ce(NO_3)_6$ and 19.2 g of urea were dissolved in 320 mL ultrapure water (resistance > 18 MΩ). The aqueous solution was refluxed for 8 h at the boiling temperature and then aged overnight at room temperature. Then the precipitates were filtered and washed several times with hot water; dried in vacuum at 80 °C for 16 h; and finally, calcined under ambient air at 650 °C for 8 h. Au/CeO_2 catalysts with various Au:CeO_2 weight ratios were prepared by a deposition−precipitation (DP) method employing $HAuCl_4$ as the Au precursor. Typically, a desired amount of $HAuCl_4$ aqueous solution, 1.0 g of CeO_2, and 50 mL of ultrapure water were coadded into a three-neck bottle and adequately mixed by stirring at 60 °C for 15 min. An appropriate amount of ammonium hydroxide was added to adjust the pH value of the system to between 8 and 8.5, after which the system was stirred at 60 °C for 1 h. The solid was then filtered, washed with ultrapure water several times, dried at 60 °C under vacuum for 12 h, and calcined at 400 °C for 2 h.

2.2. Characterization Methods. BET specific surface areas were measured using a Micromeritics Tristar II 3020 M system, and the sample was degassed at 300 °C in a nitrogen atmosphere before the measurement. The compositions of catalysts were analyzed by inductively coupled plasma atomic emission spectrometer. Powder X-ray diffraction (XRD) patterns were recorded on a Philips X'Pert PRO diffractometer using a nickel-filtered Cu Kα (wavelength: 0.15418 nm) radiation source with operation voltage and operation current of 40 kV and 40 mA, respectively. X-ray photoelectron spectroscopy (XPS) measurements were performed on an Escalab 250 high-performance electron spectrometer using monochromatized Al Kα ($h\nu$ = 1486.7 eV) as the excitation source. The likely charging of samples was corrected by setting the binding energy of the adventitious carbon (C 1s) to 284.8 eV. Transmission electron microscopy (TEM) and high-resolution transmission electron microscopy (HRTEM) experiments were preformed on JEOL-2100F with electron acceleration energy of 200 kV. X-ray absorption spectra were recorded at room temperature in the fluorescence mode at the BL14W1 beamline of Shanghai Synchrotron Radiation Facility, China.

2.3. Operando DRIFTS Experiments. Operando DRIFTS measurements were performed on a Nicolet 6700 FTIR spectrometer equipped with an in situ DRIFTS reaction cell (Harrick Scientific Products, Inc.) and a MCT/A detector. Prior to the measurements, 100 mg of catalyst was loaded onto the sample stage of the reaction cell and pretreated at 120 °C under Ar (flow rate: 20 mL/min) for 1 h to desorb adsorbed water, then cooled down to RT in Ar. In the subsequent CO adsorption experiments, the CO flow (1%CO/Ar, flow rate: 20 mL/min) was introduced onto the catalyst at RT for 1 h and then purged with Ar (flow rate: 20 mL/min) or O_2 (1%O_2/Ar, flow rate: 20 mL/min) at RT for 4 h. In the subsequent CO + O_2 reaction experiments, the CO + O_2 flow (1%CO/1%O_2/Ar, flow rate: 20 mL/min) was introduced onto the catalyst at RT for 1 h. The adsorption/reaction and purging processes were monitored by DRIFTS using the series measurement function with 64 scans and a resolution of 4 cm^{-1} that gave a temporal resolution of 24.36 s. The intensities of adsorbed species were evaluated in Kubelka−Munk units (KMU), derived from the reflectance, R_ν, via the equation of $KMU_\nu = (1 - R_\nu)^2/2R_\nu$ that was proved to be proportional to the adsorbate concentration over a wide range of experimental conditions.[28,29] Similar quantitative analysis was previously used in the DRIFTS studies of the water−gas shift reation.[30−32] The DRIFTS spectrum of the freshly pretreated catalyst purged with Ar at RT was taken as the background spectrum. The gas-phase CO signal was further subtracted using the spectrum acquired on the pure support in CO (1% CO/Ar, flow rate: 20 mL/min) atmosphere. The peak-fitting of DRIFTS spectra was processed with the peak deconvolution function of Nicolet's OMNIC Spectra Software.

2.4. CO Oxidation Experiments. Catalytic activity was evaluated with a fixed-bed flow reactor. The catalyst experienced no pretreatment prior to the catalytic reaction. The used catalyst weight was 100 mg (particle size: 280−450 μm), and the reaction gas consisting of 1% CO, 1% O_2, and 98% N_2 was fed at a space velocity of 60 000 mL g^{-1} h^{-1}. The composition of the effluent gas was detected with an online GC-^{14}C gas chromatograph equipped with a 5A column (T = 60 °C, H_2 as the carrier gas at 30 mL/min). The steady state conversion of CO was calculated from the change in CO concentrations in the inlet and outlet gases.

3. RESULTS AND DISCUSSION

Three Au/CeO_2 catalysts with Au/CeO_2 weight ratios of 0.18%, 0.97%, and 5.7% were prepared and characterized in detail. The BET specific surface areas of 0.18%-, 0.97%-, and 5.7%-Au/CeO_2 catalysts are 79.2, 71.6, and 75.2 m^2/g, respectively. In their XRD patterns (Figure 1A), all Au/CeO_2 catalysts exhibit strong CeO_2 diffraction peaks, but only 5.7%-Au/CeO_2 catalyst exhibit weak Au diffraction peaks, whereas 0.18%- and 0.97%-Au/CeO_2 catalysts do not. This could be likely due to the low Au loadings or the very fine Au particles of 0.18%- and 0.97%-Au/CeO_2 catalysts. In their TEM and HRTEM images (Figure 2 and Figures S1−S3), supported Au particles in all Au/CeO_2 catalysts exhibit similar polyhedral shapes, and their sizes are 1.7 ± 0.6, 2.6 ± 0.6, and 3.7 ± 0.9

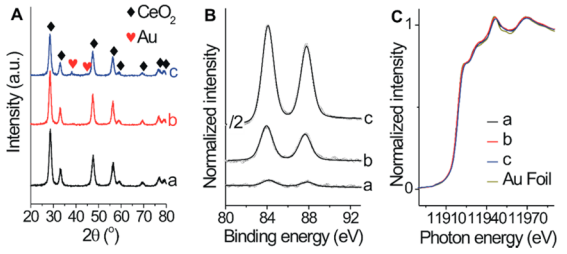

Figure 1. (A) XRD patterns, (B) Au 4f XPS, and (C) Au L_{III} edge XANES spectra of (a) 0.18%-Au/CeO_2, (b) 0.97%-Au/CeO_2, and (c) 5.7%-Au/CeO_2 catalysts.

DOI: 10.1021/cs502067x
ACS Catal. 2015, 5, 1653−1662

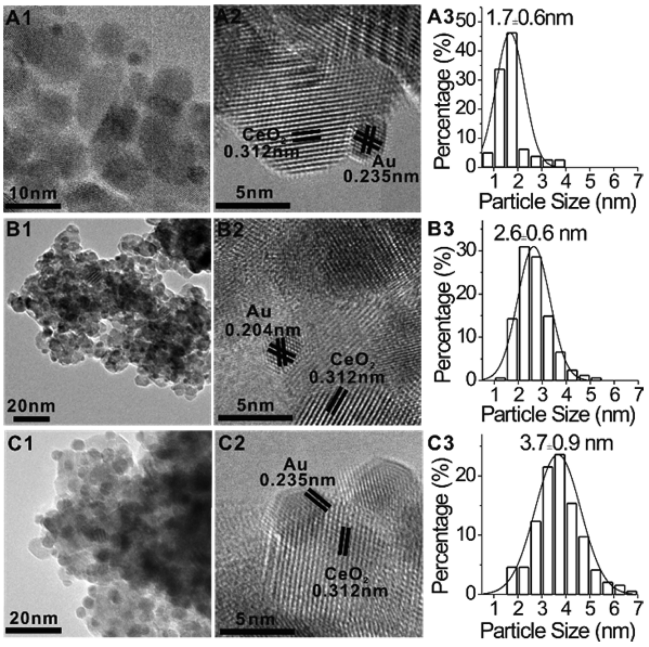

Figure 2. TEM, HRTEM images, and Au particle size distributions of (A1−A3) 0.18%-Au/CeO_2, (B1−B3) 0.97%-Au/CeO_2, and (C1−C3) 5.7%-Au/CeO_2 catalysts.

nm, respectively, in 0.18%-, 0.97%-, and 5.7%-Au/CeO_2 catalysts. In the Au 4f XPS spectra (Figure 1B), all Au/CeO_2 catalysts exhibit a single Au 4f component, with the Au $4f_{7/2}$ binding energy at 84.0 eV, a typical value for metallic Au; in the Au L_{III} edge XANES spectra (Figure 1C), all Au/CeO_2 catalysts exhibit the same white-line peak as that of Au foil. Thus, metallic Au dominates in all Au/CeO_2 catalysts. Model catalyst studies have established that the Au 4f binding energy of ultrafine Au particles will increase with a decrease in their size, and the charge transfer from reducible oxide supports to ultrafine Au nanoparticles can counteract this effect.[4,33,34] We previously observed that the Au 4f binding energy of Au particles below 2 nm supported on SiO_2 was higher than those of larger Au particles and bulk Au,[9] but Au particles below 2 nm supported on CeO_2 in 0.18%-Au/CeO_2 catalyst exhibit the same Au 4f binding energy as those larger Au particles in 0.97%- and 5.7%-Au/CeO_2 catalysts. This could be taken as an indication that charge transfer occurs between Au particles and CeO_2 support to modify the electronic structure of supported Au particles.

Figure 3A presents catalytic activity of various Au/CeO_2 catalysts in CO oxidation with the reaction gas consisting of 1% CO, 1% O_2, and 98% N_2. The various reaction rates of Au/CeO_2 catalysts at 25 °C follow the order of 5.7%-Au/CeO_2 (1.29×10^{-6} mol_{CO} $g_{catalyst}^{-1}$ s^{-1}) > 0.97%-Au/CeO_2 (3.7×10^{-7} mol_{CO} $g_{catalyst}^{-1}$ s^{-1}) > 0.18%-Au/CeO_2 (2.04×10^{-7} mol_{CO} $g_{catalyst}^{-1}$ s^{-1}), and the reaction rates normalized to the Au loading at 25 °C follow the order of 0.18%-Au/CeO_2 (22.3 $mmol_{CO}$ mol_{Au}^{-1} s^{-1}) ≫ 0.97%-Au/CeO_2 (7.5 $mmol_{CO}$ mol_{Au}^{-1} s^{-1}) > 5.7%-Au/CeO_2 (4.4 $mmol_{CO}$ mol_{Au}^{-1} s^{-1}). These results agree with the generally observed size-dependent catalytic activity of Au particles supported on CeO_2 in CO oxidation that the specific catalytic activity normalized to the Au loading increases with a decrease in the size of the Au particle. The Arrhenius plots of various Au/CeO_2 catalysts in CO oxidation were plotted employing the data in Figure 3A,

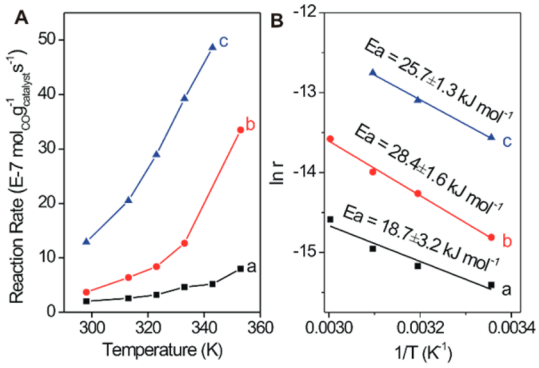

Figure 3. (A) Catalytic activity and (B) Arrhenius plots of (a) 0.18%-Au/CeO_2, (b) 0.97%-Au/CeO_2, and (c) 5.7%-Au/CeO_2 catalysts in CO oxidation.

from which the apparent activation energies were calculated. The results (Figure 3B) show that the apparent activation energies of 0.97%- and 5.7%-Au/CeO_2 are similar and larger than that of 0.18%-Au/CeO_2.

Time-resolved operando-DRIFTS spectroscopy was used to comprehensively study the CO adsorption and oxidation processes on these Au/CeO_2 catalysts. Figure 4A shows operando-DRIFTS spectra of steady-state CO adsorption on CeO_2 and Au/CeO_2 at RT employing the spectrum of the corresponding sample in Ar as the background. CO can adsorb on either Au surfaces to form adsorbed CO(a) or on CeO_2 surfaces to form carbonate, bicarbonate, and formate species. Peak-fitting was performed for these spectra for a quantitative analysis. The results are shown in Figure 4B−E, and the assignments of the observed vibrational bands are summarized in Table 1 on the basis of previous reports.[15,24,26,27,35−48] On bare CeO_2 (Figure 4B), CO adsorption leads to the formation of bidentate bicarbonate ($\nu(CO_3)$ at 1638 cm^{-1}), monodentate carbonate ($\nu(CO_3)$ at 1452 cm^{-1}), bridged carbonate ($\nu(CO_3)$ at 1417 cm^{-1}), bidentate carbonate ($\nu(CO_3)$ at 1300 and 1569 cm^{-1}), and carbonite (ν(OCO) at 1272 cm^{-1}). The formation of bidentate bicarbonate is accompanied by their ν(OH) vibrational band at 3610 cm^{-1} at the expense of the terminal isolated hydroxyl groups of CeO_2 (ν(OH) at 3735 cm^{-1}); meanwhile the bands at ∼3690 and ∼3672 cm^{-1} arising from the bridging isolated hydroxyl groups of CeO_2 also slightly increase. All these bands get significantly enhanced for CO adsorption on Au/CeO_2 catalysts and grow with the increasing Au loading (Figure 3A), and their peak positions slightly shift (Figure 4C−E). In addition, three new species—polydentate carbonate ($\nu(CO_3)$ at 1472−1481 cm^{-1}), bidentate formate (ν(OCO) at 1370−1373 cm^{-1}), and unassigned carbonate (ν(OCO) at ∼1339 cm^{-1})—were observed, and bridged formate (ν(OCO) at 1356 cm^{-1}) was observed to form on 0.18%-Au/CeO_2 but not on 0.97%- and 5.7%-Au/CeO_2. The formation of formate species on Au/CeO_2 catalysts is accompanied by a decrease in the bridging isolated hydroxyl groups at the Au/CeO_2 interface (ν(OH) at 3656 cm^{-1}). These observations demonstrate that the loading of Au particles on CeO_2 creates a large number of surface sites for CO adsorption to form carbonate, bicarbonate, and formate species and that the types and numbers of these surface sites depend on the sizes and loadings of Au particles. Reasonably, these adsorption sites should be located at the Au/CeO_2 interfaces.

In addition to carbonate, bicarbonate, and formate species involving CeO_2 surfaces, CO(a) adsorbed on Au surfaces forms

DOI: 10.1021/cs502067x
ACS Catal. 2015, 5, 1653−1662

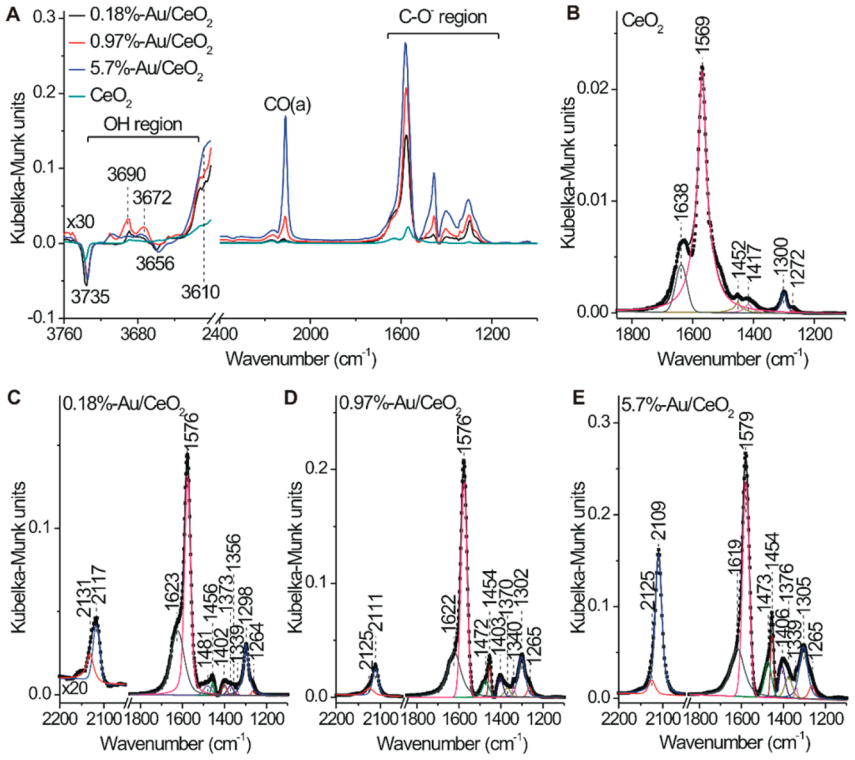

Figure 4. (A) Operando-DRIFTS spectra of steady-state CO adsorption on 0.18%-Au/CeO_2, 0.97%-Au/CeO_2, 5.7%-Au/CeO_2, and CeO_2 catalysts at RT and (B–E) their peak-fitting results. The scatter data and solid lines represent the original data and fitted curves, respectively. The signals of gas-phase CO in the as-acquired operando-DRIFTS spectra were subtracted during the peak-fitting processes.

Table 1. Assignment of Vibrational Bands Formed upon CO Adsorption on CeO_2 and Au/CeO_2 Catalysts

Assignment	Schematic structure	Bands (cm^{-1})	References
Carbonite		1264~1272	38,39
Bidentate carbonate		1298~1308 1566~1579	15,36,39-41
Unassigned carbonates	-	1337~1341	27,39
Bridged formate		1355~1358	39,41-44
Bidentate formate		1367~1376 1566~1579	27,39,43-45
Bridged carbonate		1397~1417	36,39,40
Monodentate carbonate		1452~1458	39,40
Polydentate carbonate		1472~1498	35,38,39
Bidentate bicarbonate		1618~1638	35,36,39
CO(a)-Au^0	-	2109~2118	21,24,26,37
CO(a)-$Au^{\delta+}$	-	2125~2131	
Terminal isolated OH on CeO_2		3735	35,36,45-48
Bridging isolated OH on CeO_2		3672 3690	35,36,46,47
		3647	
Bridging isolated OH on Au-CeO_2 interface		3656	-

upon CO adsorption on Au/CeO_2 catalysts and their peak intensities increase with the Au loading. The vibrational peak of CO(a) could be fitted with two components at ~2109–2117 and 2125–2131 cm^{-1} that can be assigned to CO(a) at the Au^0 and $Au^{\delta+}$ sites (Table 1), respectively. The $Au^{\delta+}$ sites were proposed to locate at the Au/CeO_2 interfaces.[49−51] The $Au^{\delta+}$/Au^0 ratio was estimated from the intensity ratio between the vibrational bands of CO(a)–$Au^{\delta+}$ and CO(a)–Au^0 as 0.70, 0.47, and 0.10, respectively, for 0.18%-, 0.97%-, and 5.7%-Au/CeO_2 (Table 2). This agrees with the fact that finer supported Au particles are more dispersed and form more fractions of Au–CeO_2 interfaces.

After steady-state CO adsorption at RT, Au/CeO_2 catalysts were then purged in Ar. and the processes were monitored with time-resolved DRIFTS spectroscopy. Figure 5A shows DRIFTS spectra after purging for 4 h employing the spectrum of the corresponding sample in Ar as the background. The peak fitting results are shown in Figure 5B–D. After purging in Ar for 4 h, the vibrational features of most surface species formed upon CO adsorption greatly weaken, demonstrating their desorption or decomposition. A very tiny vibrational peak at 2140 cm^{-1} of CO(a)–$Au^{\delta+}$ could still be observed for 0.97%- and 5.7%-Au/CeO_2, but the feature of CO(a)–Au^0 could not be observed.

Table 2. Vibrational Peak Intensities of CO(a)–Au^0 and CO(a)–$Au^{\delta+}$ Formed on Au/CeO_2 Catalysts during Steady State CO Adsorption and CO + O_2 Reaction at RT

	CO adsorption			CO+O_2 reaction		
catalyst	CO(a)–Au^0	CO(a)–$Au^{\delta+}$	CO(a)–$Au^{\delta+}$/CO(a)–Au^0	CO(a)–Au^0	CO(a)–$Au^{\delta+}$	CO(a)–$Au^{\delta+}$/CO(a)–Au^0
0.18%-Au/CeO_2	0.033	0.023	0.70	0.0196	0.0133	0.68
0.97%-Au/CeO_2	0.448	0.209	0.47	0.096	0.072	0.75
5.7%-Au/CeO_2	3.54	0.372	0.10	0	1.12	

DOI: 10.1021/cs502067x
ACS Catal. 2015, 5, 1653−1662

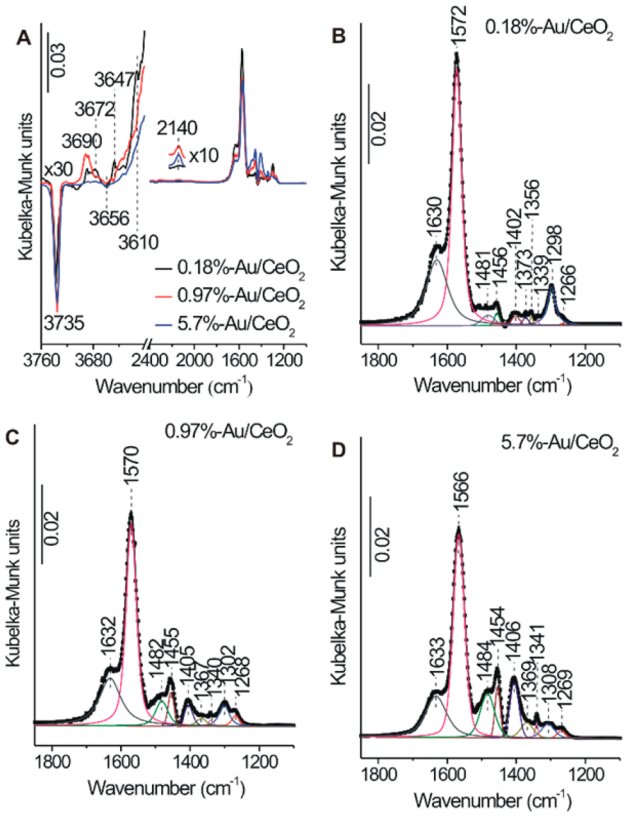

Figure 5. (A) DRIFTS spectra of Au/CeO_2 catalysts saturated by CO adsorption at RT were purged in Ar for 4 h; (B–D) their peak-fitting results. The scatter data and solid lines represent the original data and fitted curves, respectively.

This demonstrates that $CO(a)–Au^{\delta+}$ on Au/CeO_2 catalysts is more stable than $CO(a)–Au^0$, agreeing with previous results.[16] Carbonate, bicarbonate, and formate species on Au/CeO_2 formed upon CO adsorption are more stable than CO(a), as demonstrated by their much stronger vibrational features (Figure 5A). We observed that the stabilities of carbonate, bicarbonate, and formate species differed among various Au/CeO_2 catalysts. Taking the vibrational band at ~1570 cm^{-1} as an example, the order of its intensity upon CO adsorption follows 5.7%-Au/CeO_2 > 0.97%-Au/CeO_2 > 0.18%-Au/CeO_2 (Figure 4A) but becomes 0.18%-Au/CeO_2 > 0.97%-Au/CeO_2 ≈ 5.7%-Au/CeO_2 after purging for 4 h (Figure 5A). This indicates that the desorption/decomposition activity of the surface species related to ~1570 cm^{-1} (bidentate carbonate or bidentate formate) should follow the order of 5.7%-Au/CeO_2 > 0.97%-Au/CeO_2 > 0.18%-Au/CeO_2. The stretch vibrational features of hydroxyl groups vary with both the type of hydroxyl groups and the catalyst. The following observations are noteworthy: (1) the minus band (~3735 cm^{-1}) of the terminal isolated hydroxyl groups after Ar purging do not change much compared with those formed upon CO adsorption; (2) the band (~3610 cm^{-1}) of bidentate bicarbonate on 0.18%-Au/CeO_2 is stronger than that on 0.97%- and 5.7%-Au/CeO_2; (3) a new feature at ~3647 cm^{-1} assigned to the bridging isolated hydroxyl groups of CeO_2 with neigubouring oxygen vacancy (Table 1) is very obvious for the 0.18%-Au/CeO_2.

We also employed time-resolved DRIFTS spectroscopy to study the purge processes of Au/CeO_2 catalysts saturated by CO adsorption at RT in O_2, in which the surface species not only desorbed or decomposed but also were likely oxidized. Figure 6A shows DRIFTS spectra after O_2 purging for 4 h; the corresponding peak-fitting results are shown in Figure 6B–D.

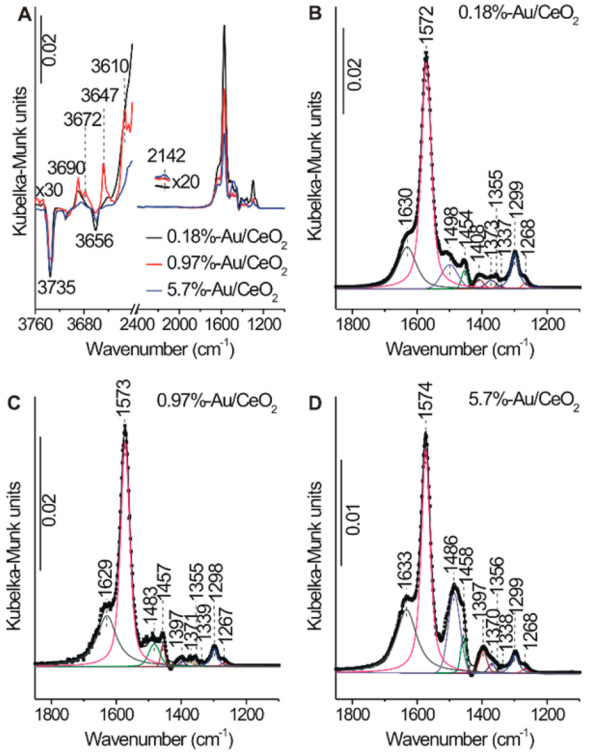

Figure 6. (A) DRIFTS spectra of Au/CeO_2 catalysts saturated by CO adsorption at RT were purged in O_2 for 4 h and (B–D) their peak-fitting results. The scatter data and solid lines represent the original data and fitted curves, respectively.

The vibrational features of CO(a) after being purged in O_2 are much weaker than those after being purged in Ar, which demonstrates the occurrence of CO(a) oxidation in addition to desorption during the O_2 purging. Comapring those purged in Ar, the vibrational features of carbonate, bicarbonate, and formate species vary with both the surface species and the catalyst. For examples, the vibrational band at ~1570 cm^{-1} after being purged in O_2 is weaker than that after being purged in Ar for all catalysts, demonstrating the occurrence of O_2-assisted decomposition in addition to desorption/decomposition during the O_2 purging; however, it can be seen clearly that the reduced intensity of this peak follows the order of 5.7%-Au/CeO_2 > 0.97%-Au/CeO_2 > 0.18%-Au/CeO_2. This indicates that the O_2-assisted decomposition activity of the surface species related to ~1570 cm^{-1} (bidentate carbonate or bidentate formate) should follow the order of 5.7%-Au/CeO_2 > 0.97%-Au/CeO_2 > 0.18%-Au/CeO_2. The vibrational peak of bridged formate at 1356 cm^{-1} absent on the CO-saturated 0.97%- and 5.7%-Au/CeO_2 was observed to emerge during the O_2 purging process, implying that the presence of O_2 should facilitate its formation. In the OH stretch vibration region, the minus ν(OH) peak (3656 cm^{-1}) of the bridging isolated hydroxyl groups at the Au/CeO_2 interface is visible for 0.18%- and 0.97%-Au/CeO_2 after being purged in O_2 but not for some catalysts after being purged in Ar; meanwhile, the ν(OH) peak (~3610 cm^{-1}) of bidentate bicarbonate on 0.97%-Au/CeO_2 after being purged in O_2 is stronger than the corresponding one after being purged in Ar. Similar to the spectrum of CO-saturated 0.18%-Au/CeO_2 purged in Ar (Figure 4A), the feature at ~3647 cm^{-1} of the

DOI: 10.1021/cs502067x
ACS Catal. 2015, 5, 1653–1662

bridging isolated hydroxyl groups of CeO_2 with a neighboring oxygen vacancy becomes very obvious for CO-saturated 0.97%-Au/CeO_2 purged in O_2. These observations suggest that the formation of bidentate bicarbonate should be accompanied by the creation of an oxygen vacancy and the formation of the bridging isolated hydroxyl groups on CeO_2 with the neighboring oxygen vacancy.

We further examined the surface species formed on Au/CeO_2 catalysts during the steady-state CO oxidation at RT employing an operando-DRIFTS spectrometer and using the spectrum of the corresponding sample in Ar as the background. The results are shown in Figure 7. Comparing those formed during the steady-state CO adsorption at RT, CO(a) formed during the steady-state CO oxidation at RT exhibits vibrational features with reduced intensities. The CO(a) vibrational features were fitted with the CO(a)−Au^0 and CO(a)−$Au^{\delta+}$ components (Figure 7B−D) whose intensities are summarized in Table 2. For 0.18%-Au/CeO_2, the CO(a)−$Au^{\delta+}$/CO(a)−Au^0 ratio during CO oxidation is similar to that during CO adsorption, indicating that the decreasing extents of CO(a)−Au^0 and CO(a)−$Au^{\delta+}$ due to CO(a) oxidation are similar. For 0.97%-Au/CeO_2, the CO(a)−$Au^{\delta+}$/CO(a)−Au^0 ratio is mcuh larger during CO oxidation than during CO adsorption, indicating that the decreasing extent of CO(a)−Au^0 due to CO(a) oxidation is much larger than that of CO(a)−$Au^{\delta+}$. For 5.7%-Au/CeO_2, no CO(a)−Au^0 component could be fitted, and the CO(a)−$Au^{\delta+}$ peak under CO oxidation is much stronger than that under CO adsorption. This observation demonstrates the creation of $Au^{\delta+}$ sites on 5.7%−Au/CeO_2 during CO oxidation at RT that can be attributed only to the presence of oxygen species on the Au surfaces. Thus, the adsorption and activation of O_2 on the Au surfaces follow the order of 5.7%-Au/CeO_2 with Au particles dominantly between 2.5 and 5 nm > 0.97%-Au/CeO_2 with Au particles dominantly between 1.5 and 3.5 nm > 0.18%-Au/CeO_2 with Au particles predominantly between 1 and 2 nm. This indicates that the optimal size of Au particles supported on CeO_2 to adsorb and activate O_2 should be within 2.5 and 5 nm, which needs further investigations. These results also demonstrate that CO(a)−Au^0 is more reactive toward O_2 than CO(a)−$Au^{\delta+}$, which is consistent with previous results.[16] This could be associated with the stronger interaction between the CO(a)−$Au^{\delta+}$ and Au surface than between the CO(a)−Au^0 and Au surface, as demonstrated in Figure 5A. These observations indicate an interesting oxygen species-induced self-poisoning of the Au surface in catalyzing low temperature CO oxidation in which the oxygen species locally results in the creation of $Au^{\delta+}$ sites and subsequently less-reactive CO(a)−$Au^{\delta+}$ species. Comparing those formed during the steady-state CO adsorption at RT, carbonate, bicarbonate, and formate species during the steady-state CO oxidation at RT exhibit vibrational features varying with the catalysts. For example, a bridged formate species with its vibrational peak at 1356 cm^{-1} absent on 0.97%- and 5.7%-$Au-CeO_2$ during CO adsorption is formed during CO oxidation, implying that the presence of O_2 should facilitate its formation. A noteworthy observation is the ν(OCO) vibrational feature of CO_2(a) on the Ce^{4+} sites of CeO_2 at 2342 cm^{-1} for 0.97%- and 5.7%-Au/CeO_2.[27,37] This directly proves that the decomposition of carbonate, bicarbonate, or formate species on the CeO_2 of 0.97%- and 5.7%-Au/CeO_2 catalysts can be facilitated by O_2 at RT to produce CO_2.

The relative coverages of major surface species on various Au/CeO_2 catalysts under different conditions at RT are quantitatively compared employing the intensities of fitted peaks in the DRIFTS spectra. As shown in Figure 8, the behaviors of CO(a) on various Au/CeO_2 catalysts are similar in which the coverage of CO(a) under steady-state CO oxidation is much smaller than that under steady-state CO adsorption, and the coverage of CO(a) after saturating CO adsorption purged in O_2 is smaller than that purged in Ar. This proves that the oxidation of CO(a) by O_2 occurs facilely at RT for all Au/CeO_2 catalysts and contributes to the observed catalytic activity in CO oxidation. However, the behaviors of carbonate, bicarbonate, and formate species vary with different Au/CeO_2 catalysts.

On 0.18%-Au/CeO_2, the coverages of monodentate carbonate, polydentate carbonate, carbonite, and bidentate formate after saturating CO adsorption purged in O_2 is not smaller than the corresponding ones purged in Ar, which demonstrates their inertness toward O_2 oxidation; meanwhile, their coverages under steady-state CO oxidation are larger than the corresponding ones under steady-state CO adsorption, which demonstrates the O_2-enhanced formation of these surface species. These observations suggest that monodentate carbonate, polydentate carbonate, carbonite, and bidentate formate will accumulate on 0.18%-Au/CeO_2 during CO oxidation at RT and act as the spectators and even likely block active surface sites. The coverage of bridged carbonate after saturating CO adsorption purged in O_2 is smaller than that purged in Ar, which demonstrates their activity toward O_2 oxidation; however, its coverage under steady-state CO oxidation is slightly larger than that under steady-state CO

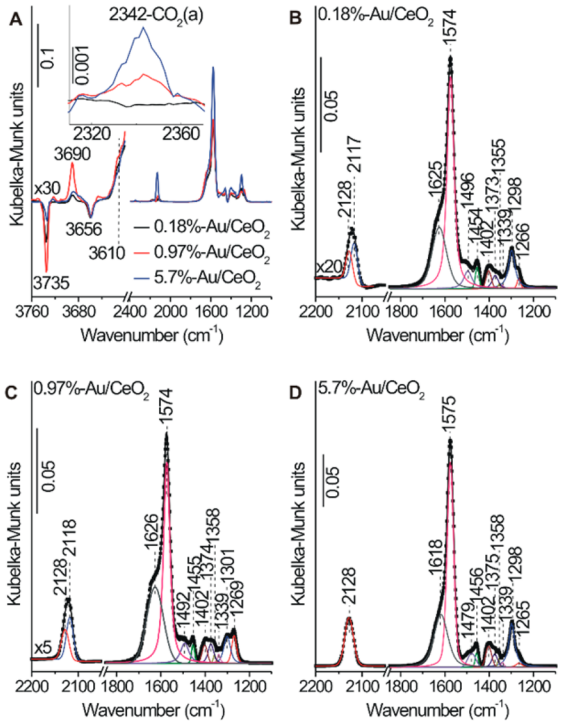

Figure 7. (A) Operando-DRIFTS spectra of steady-state CO oxidation on Au/CeO_2 catalysts at RT and (B−D) their peak-fitting results. The inset in Figure 6A shows the amplified region for CO_2(a) on Ce^{4+} sites. The scatter data and solid lines represent the original data and fitted curves, respectively. The signals of gas-phase CO in the as-acquired operando-DRIFTS spectra were subtracted during the peak-fitting processes.

DOI: 10.1021/cs502067x
ACS Catal. 2015, 5, 1653−1662

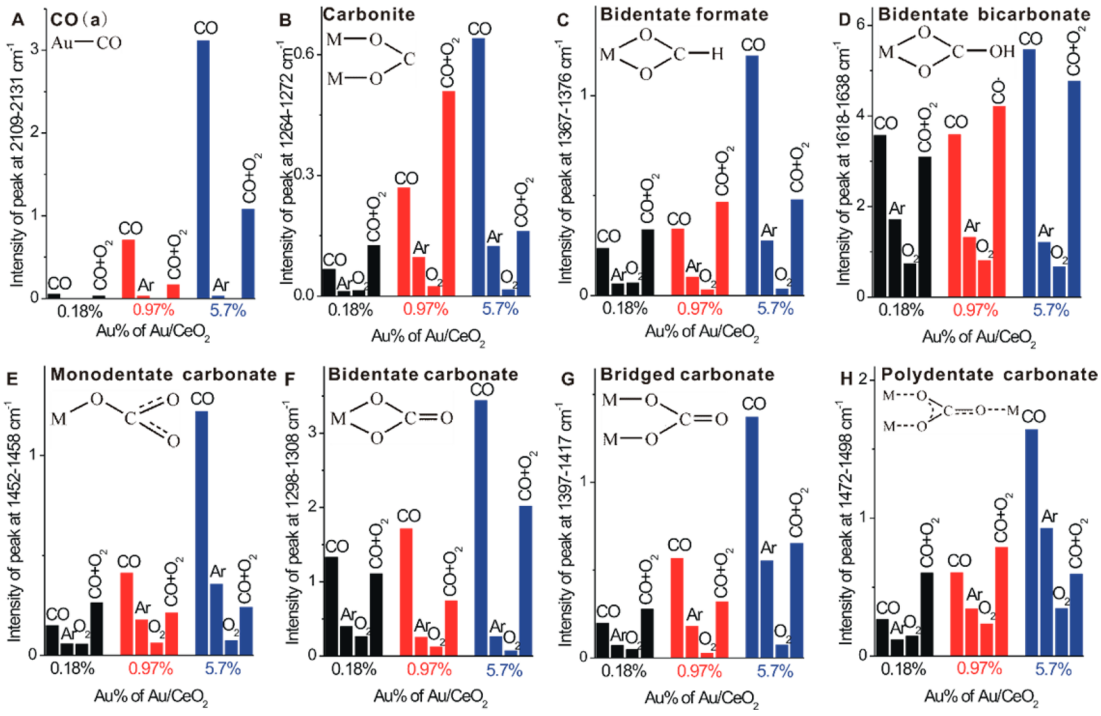

Figure 8. Integrated vibrational peak intensities of major surface species formed on various Au/CeO_2 catalysts under different conditions at RT.

adsorption. This demonstrates that the O_2-enhanced formation rate of bridged carbonate is faster than its oxidation rate on 0.18%-Au/CeO_2 during CO oxidation at RT. Thus, bridged carbonate is an active surface species on 0.18%-Au/CeO_2 during CO oxidation at RT but will accumulate on the surface and likely suppress the formation of other more active surface species. The coverages of bidentate carbonate and bidentate bicarbonate after saturating CO adsorption purged in O_2 are smaller than the corresponding ones purged in Ar, and those under steady-state CO oxidation are smaller than the corresponding ones under steady-state CO adsorption. Therefore, bidentate carbonate and bidentate bicarbonate are active surface species on 0.18%-Au/CeO_2 during CO oxidation at RT and do not interfere with other active surface species.

On 0.97%-Au/CeO_2, the coverages of all studied carbonate, bicarbonate, and formate species after saturating CO adsorption purged in O_2 are smaller than the corresponding ones purged in Ar, which demonstrates their activity toward O_2 oxidation; however, the coverages of monodentate carbonate, bidentate carbonate, and bridged carbonate under steady-state CO oxidation are smaller than the corresponding ones under steady-state CO adsorption, whereas those of polydentate carbonate, carbonite, bidentate formate, and bidentate bicarbonate are larger than the corresponding ones under steady-state CO adsorption. Therefore, all these surface species are active surface species on 0.97%-Au/CeO_2 during CO oxidation at RT, and monodentate carbonate, bidentate carbonate, and bridged carbonate do not interfere with other active surface species, but polydentate carbonate, carbonite, bidentate formate, and bidentate bicarbonate will accumulate on the surface and likely suppress the formation of other more active surface species.

On 5.7%-Au/CeO_2, the coverages of all studied carbonate, bicarbonate, and formate species after saturating CO adsorption purged in O_2 are smaller than the corresponding ones purged in Ar, which demonstrates their activity toward O_2 oxidation; moreover, the coverages of all studied carbonate, bicarbonate, and formate species under steady-state CO oxidation are smaller than the corresponding ones under steady-state CO adsorption. Therefore, all these surface species are active surface species on 5.7%-Au/CeO_2 during CO oxidation at RT and do not interfere with other active surface species.

The above results clearly demonstrate that the formation, decomposition activity, and role of carbonate, bicarbonate, and formate species on Au/CeO_2 catalysts in CO oxidation at RT depend on the Au particle size. Within the size ranges of Au particles supported on CeO_2 in the present study, more types of carbonate, bicarbonate, and formate species become active toward O_2-assisted decomposition on larger supported Au particles, and thus, more surface species and related oxidation pathways contribute to the catalytic activity of these Au/CeO_2 catalysts in CO oxidation at RT. Because the formation and decomposition of carbonate, bicarbonate, and formate species on CeO_2 are generally relevant to the reactivity of surface lattice oxygen, our results indicate that within the studied sizes large Au particles supported on CeO_2 should be more capable of activating the surface lattice oxygen of CeO_2 than fine Au particles.

We also quantitatively compared the intrinsic oxidation/decomposition reactivity of major surface species on various Au/CeO_2 catalysts on the basis of time-resolved DRIFTS results for the purging processes in Ar and O_2 after saturating CO adsorption at RT. Figure 9 shows time-resolved DRIFTS spectra at selected times during the purging processes. Figure 10 shows variations of the normalized intensity of various vibrational peaks as a function of the time during the initial purging processes, which reflect the intrinsic oxidation/decomposition reactivity of corresponding species. The results for the whole purging processes are shown in Figures S4, S5. During the initial process of Ar purging, the normalized vibrational peak intensities of CO(a), carbonate, bicarbonate, and formate species on various Au/CeO_2 catalysts exhibit

DOI: 10.1021/cs502067x
ACS Catal. 2015, 5, 1653−1662

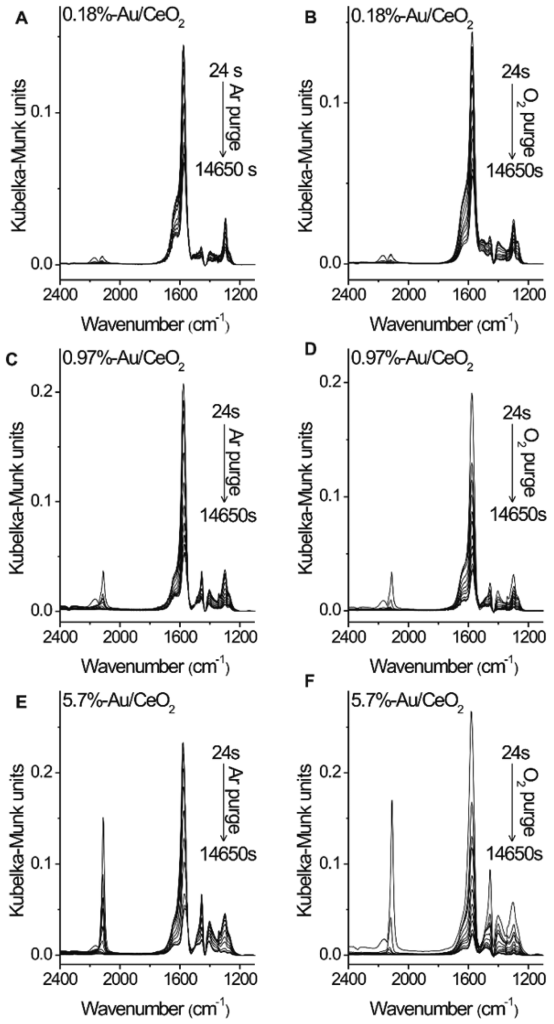

Figure 9. Time-resolved DRIFTS spectra at selected times during the Ar and O_2 purging processes of various Au/CeO_2 catalysts saturated by CO adsorption at RT.

similar decreasing rates, indicating that the intrinsic desorption/decomposition activity of these surface species on Au/CeO_2 catalysts do not depend much on the size of supported Au particles. However, during the initial process of O_2 purging, their normalized vibrational peak intensities on various Au/CeO_2 catalysts exhibit distinctly different behaviors. The normalized vibrational peak intensities of CO(a) on Au/CeO_2 catalysts decrease faster during the O_2 purging process than during the Ar purging process, demonstrating the occurrence of the CO(a) oxidation reaction in addition to the desorption of CO(a) during O_2 purging; meanwhile, the normalized vibrational peak intensities of CO(a) on Au/CeO_2 catalysts exhibit similar decreasing rates during the initial O_2 purging process, suggesting that the intrinsic oxidation reactivity of CO(a) on a Au particle supported on CeO_2 by O_2 does not depend much on their sizes.

The normalized vibrational peak intensity of carbonite on 0.18%-Au/CeO_2 initially increases and then decreases slowly during the O_2 purging process, whereas that on 5.7%-Au/CeO_2 keeps decreasing, and the behavior of carbonite on 0.97%-Au/CeO_2 lies between those on 0.18%-$Au/CeO_2$and 5.7%-Au/CeO_2. The initial increase of the carbonite coverage on 0.18%-Au/CeO_2 can be attributed to the O_2-assisted formation of carbonite with the presence of CO in the gas phase during the initial O_2 purging process. These observations demonstrate the size-dependent O_2-assisted formation ($r_{formation}$) of carbonite and its intrinsic decomposition reactivity ($r_{decomposition}$) on Au/CeO_2 catalysts. The $r_{formation}$ and $r_{decomposition}$ of carbonite on various Au/CeO_2 catalysts follow the order of $r_{formation} \gg r_{decomposition}$ for 0.18%-Au/CeO_2 with Au sizes of 1.7 ± 0.6 nm, $r_{formation} \approx r_{decomposition}$ for 0.97%-Au/CeO_2 with Au sizes of 2.6 ± 0.6 nm, and $r_{formation} \ll r_{decomposition}$ for 5.7%-Au/CeO_2 with Au sizes of 3.7 ± 0.9 nm. These results are consistent with the above results that the coverage of carbonite formed on 0.18%-Au/CeO_2 and 0.97%-Au/CeO_2 under the steady state CO + O_2 reaction is higher than under the steady state CO adsorption, whereas that on 5.7%-Au/CeO_2 under the steady state CO + O_2 reaction is lower than under the steady state CO adsorption (Figure 8B). Bidentate formate, bidentate bicarbonate, and polydentate carbonate on Au/CeO_2 catalysts during the O_2 purging process exhibit behavior similar to that of carbonite.

The normalized vibrational peak intensities of monodentate carbonate and bridged carbonate on Au/CeO_2 catalysts vary similarly during the initial O_2 purging process. The $r_{formation}$ and $r_{decomposition}$ of monodentate carbonate and bridged carbonate are similar on 0.18%-Au/CeO_2; however, their normalized vibrational peak intensities for 0.97%-Au/CeO_2 and 5.7%-Au/CeO_2 initially decrease quickly and similarly, demonstrating that their intrinsic decomposition reactivities are greatly enhanced with the Au particle sizes increasing from 1.7 ± 0.6 nm to 2.6 ± 0.6 and 3.7 ± 0.9 nm and do not depend much on the sizes. These results are consistent with the above results that the coverage of monodentate carbonate and bridged carbonate formed on 0.18%-Au/CeO_2 under the steady state CO + O_2 reaction is higher than under the steady state CO adsorption, whereas that on 5.7%-Au/CeO_2 and 0.97%-Au/CeO_2 under the steady state CO + O_2 reaction is lower than under the steady state CO adsorption (Figure 8E,G). Bidentate carbonate is the only surface species whose initial normalized vibrational peak intensities decrease quickly and similarly for all Au/CeO_2 catalysts. This demonstrates that the intrinsic decomposition reactivity of bidentate carbonate on Au/CeO_2 catalysts is high and does not depend much on the sizes of Au particles. These results are consistent with the above results that the coverage of bidentate carbonate formed on all Au/CeO_2 catalysts under steady state CO + O_2 reaction is lower than under the steady state CO adsorption (Figure 8F). Therefore, carbonate, bicarbonate, and formate species formed on Au/CeO_2 catalysts during CO oxidation at RT exhibit sensitively size-dependent intrinsic decomposition reactivities that increase with the Au particle size.

Our DRIFTS results of various Au/CeO_2 catalysts for CO oxidation at RT provide a comprehensive understanding of the size effect of supported Au particles on the catalytic activity in termes of the concentration and intrinsic oxidation/decomposition reactivity of various surface species, which can be summarized as the size-dependent contributions of different reaction pathways to CO oxidation. Within the studied sizes of supported Au particles ranging from 1.7 ± 0.6 nm to 3.7 ± 0.9 nm, the size of Au particles supported on CeO_2 does not affect the intrinsic oxidation reactivity of CO(a) much; thus, the size effect of supported Au particles on CO(a) oxidation is to affect the specific density of surface adsorption sites on Au particles and, subsequently, the concentration of CO(a). However, the size of Au particles supported on CeO_2 strongly affects the intrinsic decomposition reactivity of carbonate, bicarbonate, and formate species that increase with the Au particle size.

DOI: 10.1021/cs502067x
ACS Catal. 2015, 5, 1653−1662

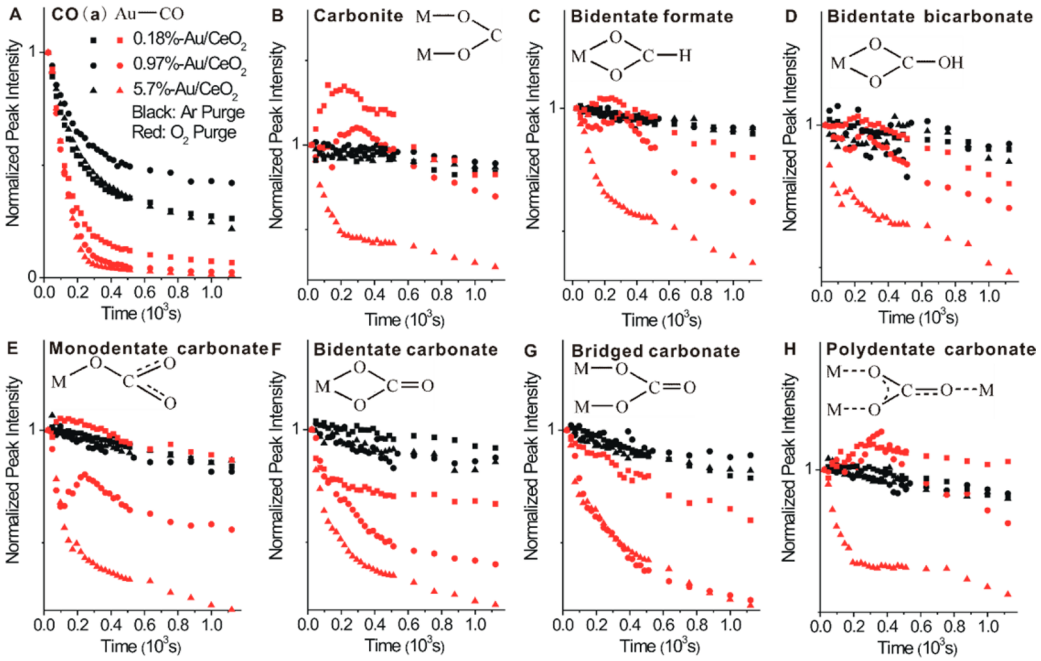

Figure 10. Variations of the normalized vibrational peak intensities of major surface species formed on various Au/CeO_2 catalysts upon saturating CO adsorption at RT as a function of time during the initial purging processes in Ar and O_2.

Thus, the size effect of supported Au particles on their decomposition is to open the CO oxidation reaction pathways involving carbonate, bicarbonate, and formate species over Au/CeO_2 catalysts with large supported Au particles and, meanwhile, to prevent the accumulation of carbonate, bicarbonate, and formate species on the catalyst surface. Therefore, the catalytic activity of 0.18%-Au/CeO_2 with Au particles of 1.7 ± 0.6 nm in CO oxidation at RT is mainly contributed by the reaction pathway of CO(a) oxidation, and carbonate, bicarbonate, and formate species are the spectators and even likely block the active sites.

The catalytic activity of 5.7%-Au/CeO_2 with Au particles of 3.7 ± 0.9 nm in CO oxidation at RT is contributed not only by the reaction pathway of CO(a) oxidation but also by the reaction pathways of carbonate, bicarbonate, and formate species. We could not quantitatively determine the contributions of the oxidation of CO(a) and the decomposition of carbonate, bicarbonate, and formate species to the catalytic activity of 5.7%-Au/CeO_2 in CO oxidation at RT, but because of the much higher stability of carbonate, bicarbonate, and formate species than CO(a), the contribution of the decomposition of carbonate, bicarbonate, and formate species to the catalytic activity of Au/CeO_2 in CO oxidation can be expected to increase with the reaction temperature.

4. CONCLUSIONS

Via a comprehensive time-resolved operando-DRIFTS study of the evolutions of various surface species on Au/CeO_2 catalysts with Au particle sizes ranging from 1.7 ± 0.6 to 3.7 ± 0.9 nm during CO oxidation at RT, we have successfully demonstrated a novel vision on the size effect in supported Au catalysts for CO oxidation in which the catalytic activity is contributed by the size-dependent different reaction pathways. CO(a), carbonate, bicarbonate, and formate species formed on Au/CeO_2 catalysts upon CO adsorption and the formation of carbonate, bicarbonate, and formate species are facilitated by the presence of O_2. The intrinsic oxidation reactivity of CO(a) is not affected much by the size of the supported, but the intrinsic decomposition reactivity of carbonate, bicarbonate, and formate species increase with the size of supported Au particle size. The size effect of supported Au particles on CO(a) oxidation is to affect the specific density of surface adsorption sites on Au particles for CO(a), and the size effect of supported Au particles on the decomposition of carbonate, bicarbonate, and formate species is to open their decomposition reaction pathways over Au/CeO_2 catalysts with large supported Au particles. The catalytic activity of Au/CeO_2 with Au particles of 1.7 ± 0.6 nm in CO oxidation at RT is contributed by the reaction pathway of CO(a) oxidation, and carbonate, bicarbonate, and formate species are the spectators and even likely block active sites. The catalytic activity of Au/CeO_2 with Au particles of 3.7 ± 0.9 nm in CO oxidation at RT is contributed not only by the reaction pathway of CO(a) oxidation but also by the reaction pathways of carbonate, bicarbonate, and formate species.

■ ASSOCIATED CONTENT

Supporting Information

The following file is available free of charge on the ACS Publications website at DOI: 10.1021/cs502067x.

Additional TEM images of various Au/CeO_2 catalysts (Figures S1–S3) and variations of the normalized vibrational peak intensities of various surface species formed on various Au/CeO_2 catalysts upon saturating CO adsorption at RT as a function of time during the whole purging processes in Ar and O_2 (Figures S4, S5) (PDF)

■ AUTHOR INFORMATION

Corresponding Author

*E-mail: huangwx@ustc.edu.cn.

Notes

The authors declare no competing financial interests.

DOI: 10.1021/cs502067x
ACS Catal. 2015, 5, 1653–1662

■ ACKNOWLEDGMENTS

This work was financially supported by the National Basic Research Program of China (2013CB933104), National Natural Science Foundation of China (U1332113, 21373192, 20973161), MOE Fundamental Research Funds for the Central Universities (WK2060030017), Collaborative Innovation Center of Suzhou Nano Science and Technology, and Strategic Priority Research Program of Chinese Academy of Sciences (XDA09030103).

■ REFERENCES

(1) Haruta, M.; Yamada, N.; Kobayashi, T.; Iijima, S. *J. Catal.* **1989**, *115*, 301−309.
(2) Haruta, M.; Tsubota, S.; Kobayashi, T.; Kageyama, H.; Genet, M. J.; Delmon, B. *J. Catal.* **1993**, *144*, 175−192.
(3) Valden, M.; Lai, X.; Goodman, D. W. *Science* **1998**, *281*, 1647−1650.
(4) Meyer, R.; Lemire, C.; Shaikhutdinov, S. K.; Freund, H. *Gold Bull.* **2004**, *37*, 72−124.
(5) Haruta, M. *Faraday Discuss.* **2011**, *152*, 11−32.
(6) Zanella, R.; Giorgio, S.; Shin, C.-H.; Henry, C. R.; Louis, C. *J. Catal.* **2004**, *222*, 357−367.
(7) Tai, Y.; Yamaguchi, W.; Tajiri, K.; Kageyama, H. *Appl. Catal., A* **2009**, *364*, 143−149.
(8) Falsig, H.; Hvolbæk, B.; Kristensen, I. S.; Jiang, T.; Bligaard, T.; Christensen, C. H.; Nørskov, J. K. *Angew. Chem., Int. Ed.* **2008**, *47*, 4835−4839.
(9) Qian, K.; Luo, L.; Bao, H.; Hua, Q.; Jiang, Z.; Huang, W. *Catal. Sci. Technol.* **2013**, *3*, 679−687.
(10) Haruta, M. *CATTECH* **2002**, *6*, 102−115.
(11) Henao, J. D.; Caputo, T.; Yang, J. H.; Kung, M. C.; Kung, H. H. *J. Phys. Chem. B* **2006**, *110*, 8689−8700.
(12) Kotobuki, M.; Leppelt, R.; Hansgen, D. A.; Widmann, D.; Behm, R. J. *J. Catal.* **2009**, *264*, 67−76.
(13) Widmann, D.; Behm, R. J. *Angew. Chem., Int. Ed.* **2011**, *50*, 10241−10245.
(14) Green, I. X.; Tang, W.; Neurock, M.; Yates, J. T., Jr. *Science* **2011**, *333*, 736−739.
(15) Romero-Sarria, F.; Martínez T, L. M.; Centeno, M. A.; Odriozola, J. A. *J. Phys. Chem. C* **2007**, *111*, 14469−14475.
(16) Manzoli, M.; Boccuzzi, F.; Chiorino, A.; Vindigni, F.; Deng, W. L.; Flytzani-Stephanopoulos, M. *J. Catal.* **2007**, *245*, 308−315.
(17) Widmann, D.; Leppelt, R.; Behm, R. J. *J. Catal.* **2007**, *251*, 437−442.
(18) Qian, K.; Lv, S.; Xiao, X.; Sun, H.; Lu, J.; Luo, M.; Huang, W. *J. Mol. Catal. A* **2009**, *306*, 40−47.
(19) Kung, M. C.; Davis, R. J.; Kung, H. H. *J. Phys. Chem. C* **2007**, *111*, 11767−11775.
(20) Daniells, S.; Overweg, A.; Makkee, M.; Moulijn, J. *J. Catal.* **2005**, *230*, 52−65.
(21) Li, M.; Wu, Z.; Ma, Z.; Schwartz, V.; Mullins, D. R.; Dai, S.; Overbury, S. H. *J. Catal.* **2009**, *266*, 98−105.
(22) Li, M. J.; Wu, Z. L.; Overbury, S. H. *J. Catal.* **2011**, *278*, 133−142.
(23) Widmann, D.; Liu, Y.; Schuth, F.; Behm, R. J. *J. Catal.* **2010**, *276*, 292−305.
(24) Li, L.; Wang, A.; Qiao, B.; Lin, J.; Huang, Y.; Wang, X.; Zhang, T. *J. Catal.* **2013**, *299*, 90−100.
(25) Qian, K.; Zhang, W.; Sun, H.; Fang, J.; He, B.; Ma, Y.; Jiang, Z.; Wei, S.; Yang, J.; Huang, W. *J. Catal.* **2011**, *277*, 95−103.
(26) Boccuzzi, F.; Chiorino, A.; Tsubota, S.; Haruta, M. *J. Phys. Chem.* **1996**, *100*, 3625−3631.
(27) Tabakova, T.; Boccuzzi, F.; Manzoli, M.; Andreeva, D. *Appl. Catal., A* **2003**, *252*, 385−397.
(28) Hamadeh, I. M.; Griffiths, P. R. *Appl. Spectrosc.* **1987**, *41*, 682−688.
(29) Sirita, J.; Phanichphant, S.; Meunier, F. C. *Anal. Chem.* **2007**, *79*, 3912−3918.
(30) Leppelt, R.; Schumacher, B.; Plzak, V.; Kinne, M.; Behm, R. J. *J. Catal.* **2006**, *244*, 137−152.
(31) Abd El-Moemen, A.; Karpenko, A.; Denkwitz, Y.; Behm, R. J. *J. Power Sources* **2009**, *190*, 64−75.
(32) El-Moemen, A. A.; Kucerova, G.; Behm, R. J. *Appl. Catal., B* **2010**, *95*, 57−70.
(33) Chusuei, C. C.; Lai, X.; Luo, K.; Goodman, D. W. *Top. Catal.* **2001**, *14*, 71−83.
(34) Jiang, Z.; Zhang, W.; Jin, L.; Yang, X.; Xu, F.; Zhu, J.; Huang, W. *J. Phys. Chem. C* **2007**, *111*, 12434−12439.
(35) Binet, C.; Daturi, M.; Lavalley, J.-C. *Catal. Today* **1999**, *50*, 207−225.
(36) Pozdnyakova, O.; Teschner, D.; Wootsch, A.; Krohnert, J.; Steinhauer, B.; Sauer, H.; Toth, L.; Jentoft, F.; Knopgericke, A.; Paal, Z. *J. Catal.* **2006**, *237*, 1−16.
(37) Boccuzzi, F.; Chiorino, A.; Manzoli, M.; Andreeva, D.; Tabakova, T. *J. Catal.* **1999**, *188*, 176−185.
(38) Binet, C.; Badri, A.; Boutonnet-Kizling, M.; Lavalley, J.-C. *J. Chem. Soc., Faraday Trans.* **1994**, *90*, 1023−1028.
(39) Vayssilov, G. N.; Mihaylov, M.; Petkov, P. S.; Hadjiivanov, K. I.; Neyman, K. M. *J. Phys. Chem. C* **2011**, *115*, 23435−23454.
(40) Li, C.; Sakata, Y.; Arai, T.; Domen, K.; Maruya, K.-i.; Onishi, T. *J. Chem. Soc., Faraday Trans. 1* **1989**, *85*, 929−943.
(41) Li, C.; Sakata, Y.; Arai, T.; Domen, K.; Maruya, K.-i.; Onishi, T. *J. Chem. Soc., Faraday Trans. 1* **1989**, *85*, 1451−1461.
(42) Li, H.-F.; Zhang, N.; Chen, P.; Luo, M.-F.; Lu, J.-Q. *Appl. Catal., B* **2011**, *110*, 279−285.
(43) Chen, B.-B.; Shi, C.; Crocker, M.; Wang, Y.; Zhu, A.-M. *Appl. Catal., B* **2013**, *132*−*133*, 245−255.
(44) Li, C.; Domen, K.; Maruya, K.-i.; Onishi, T. *J. Catal.* **1990**, *125*, 445−455.
(45) Jacobs, G.; Williams, L.; Graham, U.; Thomas, G. A.; Sparks, D. E.; Davis, B. H. *Appl. Catal., A* **2003**, *252*, 107−118.
(46) Badri, A.; Binet, C.; Lavalley, J.-C. *J. Chem. Soc., Faraday Trans.* **1996**, *92*, 4669−4673.
(47) Pozdnyakova, O.; Teschner, D.; Wootsch, A.; Kröhnert, J.; Steinhauer, B.; Sauer, H.; Toth, L.; Jentoft, F. C.; Knop-Gericke, A.; Paál, Z.; Schlögl, R. *J. Catal.* **2006**, *237*, 17−28.
(48) Laachir, A.; Perrichon, V.; Badri, A.; Lamotte, J.; Catherine, E.; Lavalley, J. C.; El Fallah, J.; Hilaire, L.; Le Normand, F.; Quemere, E.; Sauvion, G. N.; Touret, O. *J. Chem. Soc., Faraday Trans.* **1991**, *87*, 1601−1609.
(49) Longo, A.; Liotta, L. F.; Pantaleo, G.; Giannici, F.; Venezia, A. M.; Martorana, A. *J. Phys. Chem. C* **2012**, *116*, 2960−2966.
(50) Boronat, M.; Concepción, P.; Corma, A. *J. Phys. Chem. C* **2009**, *113*, 16772−16784.
(51) Bond, G.; Thompson, D. *Gold Bull.* **2000**, *33*, 41−50.

DOI: 10.1021/cs502067x
ACS Catal. 2015, 5, 1653−1662